# Modeling inductive radio frequency coupling in powerful negative hydrogen ion sources: validating a self-consistent fluid model

Dominikus Zielke, Stefan Briefi, Stiliyan Lishev, Ursel Fantz

# Modeling inductive radio frequency coupling in powerful negative hydrogen ion sources: validating a self-consistent fluid model

## D Zielke[1] , S Briefi[1] , S Lishev[2] and U Fantz[1,3]

[1] Max-Planck-Institut für Plasmaphysik, Boltzmannstr. 2, 85748 Garching, Germany
[2] Faculty of Physics, Sofia University, 1164 Sofia, Bulgaria
[3] AG Experimentelle Plasmaphysik, Universität Augsburg, 86135 Augsburg, Germany

E-mail: dominikus.zielke@ipp.mpg.de

## Abstract

Radio frequency (RF) negative hydrogen ion sources utilized in fusion and for accelerators use inductively coupled plasmas, which are operated at a low driving frequency, high power densities and gas pressures in the order of 1 MHz, 10 W cm$^{-3}$ and 1 Pa, respectively. In this work a numerical fluid model is developed for a self-consistent description of the RF power coupling in these discharges. After validating the RF power coupling mechanism, such a model is a valuable tool for the optimization of RF power coupling and hence can help to increase the efficiency and reliability of RF ion sources. The model validation is achieved using measurements from the ITER RF prototype ion source. Steady state numerical solutions are obtained for the first time, where all modeled trends fit well. Remaining systematic quantitative differences could be caused by 3D effects such as highly non-uniform magnetic fields that cannot be captured in the current model formulation, which is 2D cylindrically symmetric. The coupling between the RF fields and the electrons is realized in the electron momentum transport equation, where approximations consistent with the operating regime of RF ion sources are applied. Here large magnetic RF fields lead to a plasma compression by the nonlinear RF Lorentz force. Using a local approximation for the electron viscosity, it is found that increased diffusion of the RF current density mitigates the compression. Navier–Stokes equations for the neutral atoms and molecules are used to capture neutral depletion. In this way it is shown that at high powers neutral depletion has a large impact on the power coupling via the viscosity of the electrons. The application of the self-consistent model for optimization of the RF power coupling will be described in a forthcoming paper.

Keywords: inductively coupled plasma, RF negative hydrogen ion source, power transfer efficiency, neutral depletion, predictive self-consistent fluid model, nonlinear RF Lorentz force and viscosity, electron heating skin effect regimes

(Some figures may appear in colour only in the online journal)

---

## 1. Introduction

Radio frequency (RF) negative hydrogen or deuterium ion sources are used in fusion science [1–3] as well as for particle accelerators [4–6]. In both applications an RF generator operating at a driving frequency in the order of 1 MHz is connected via a matching network to an RF coil which is either inside or wrapped around a dielectric cylinder with typical diameters of 1–30 cm, called driver. A low temperature plasma at pressures in the order of 1 Pa is sustained in the driver by inductive coupling. In fusion applications an internal Faraday shield is present to avoid plasma erosion of the dielectric wall and hence providing stable hydrogen atomic densities to enhance the surface production of negative ions [7]. Also often present are highly non-uniform 3D magnetic cusp fields to increase the plasma confinement and magnetic filter fields in front of the extraction grid system to decrease the number of co-extracted electrons [8]. Large applied RF powers of up to 100 kW (corresponding to power densities of 10 W cm$^{-3}$) are associated with large currents and voltages at the RF coil well above 100 A and 10 kV, respectively. The high coil voltages make electric arcs likely, which decreases the reliability of the ion source. Hence the *RF coil voltage* $U_{\text{coil}}$ is a figure of merit to assess the reliability of the ion source. Not all of the RF power is coupled to the plasma but a substantial part is lost in the RF network, where heat is produced by Joule heating and eddy currents, making additional cooling of the components necessary. To quantify the RF power coupling, the figure of merit *RF power transfer efficiency*

$$\eta = \frac{P_{\text{pl}}}{P_{\text{RF}}}, \tag{1}$$

is used. Herein $P_{\text{pl}}$ is the power absorbed by the plasma and $P_{\text{RF}}$ is the total power provided by the RF generator. Various external parameters such as driving frequency, applied power, filling pressure, magnetic fields, as well as discharge and coil geometry affect $U_{\text{coil}}$ and $\eta$ in a non-trivial way.

Systematically investigating the broad parameter space experimentally is a huge effort. Moreover, the diagnostic access in RF ion source drivers is limited and hence important effects (e.g. related to the electromagnetic fields) cannot be studied easily. At the ITER prototype RF ion source, where $\eta$ has been determined for the first time, it was found to be globally below 65%, leaving a considerable optimization potential [9]. This is in reasonable agreement with the recently determined value of around 50% in the SPIDER RF negative ion source [10]. In other RF ion sources no measurements of $U_{\text{coil}}$ and $\eta$ have been reported up to now [3–6].

The experimental difficulties make it necessary to use numerical models for studying the power coupling in RF ion sources. The modeling challenges result from the applied driving frequencies, which are low compared to the industry standard frequency of 13.56 MHz, the high applied RF powers and the low filling pressures.

Within the last decade a significant amount of literature has been developed on the topic of RF power coupling in low pressure inductively coupled plasmas as well as works

that specifically target to describe the discharge regime of the RF negative ion source. Theoretical studies about nonlinear effects that become relevant only at the low driving frequencies (and are even further enhanced by the high power densities) such as the ponderomotive force and higher harmonics were performed in [11–16]. Here it was found that a large magnetic RF field causes a large RF Lorentz force, which in turn compresses the plasma. This is considered in fluid models trying to describe RF ion sources [17, 18]. Another complicating issue is the description of the heating regime at low pressures and large RF magnetic fields, where it is not clear whether only collisional heating or also stochastic heating should be involved, depending on the skin effect regime [17, 19, 20]. Also owing to the low pressures, depletion of the neutrals strongly affects the discharge behavior, as investigated in [21, 22].

There are several models available that describe the RF power coupling in ion sources. However, all these models are not self-consistent. For example, in [23, 24] the electron density and temperature are taken as uniform inputs and a cold plasma approximation [20] without accounting for the nonlinear effects is applied. For the RF coupling a transformer model [25], combined with the anomalous skin effect regime [26], is used. In contrast to that [27] used a fluid model to calculate the spatially resolved plasma parameters as well as the RF fields. However, also in this work the cold plasma approximation is used and nonlinear effects are neglected. Regarding the neutrals, a simplified description is applied, wherefore neutral depletion is not described self-consistently. Another fluid model was developed in [17, 18]. Here the neutral atoms and molecules are modeled as fluids. Detailed investigations regarding the impact of the neutral description on the discharged parameters were performed in [21] using this model. The RF power coupling is modeled using a momentum transport equation for the electrons, where stochastic heating is accounted for by means of an effective viscosity [17, 28, 29]. However, since in this approach the RF timescale is fully resolved, it was not possible to run the model until the neutrals reach a steady state, wherefore a constant neutral background had to be assumed. Furthermore, the RF Lorentz force was found to compress the plasma strongly and pushing it out of the driver, wherefore no steady state solution was obtained at 1 MHz. Hence the published results are at 10 MHz [17]. However, the effect of the nonlinear RF Lorentz force is small at 10 MHz. Beyond the apparent shortcomings of the models described above regarding the RF coupling, none of them can be considered predictive, since they all have in common that they are not validated against experimental measurements.

The special feature of the model presented in this work is that the RF power coupling is described self-consistently. This means that the macroscopic transport quantities such as neutral and plasma densities, velocities and temperatures as well as the electromagnetic fields are calculated in space and time using appropriate formulations for the RF coupling in the regime where negative ion sources typically operate. To
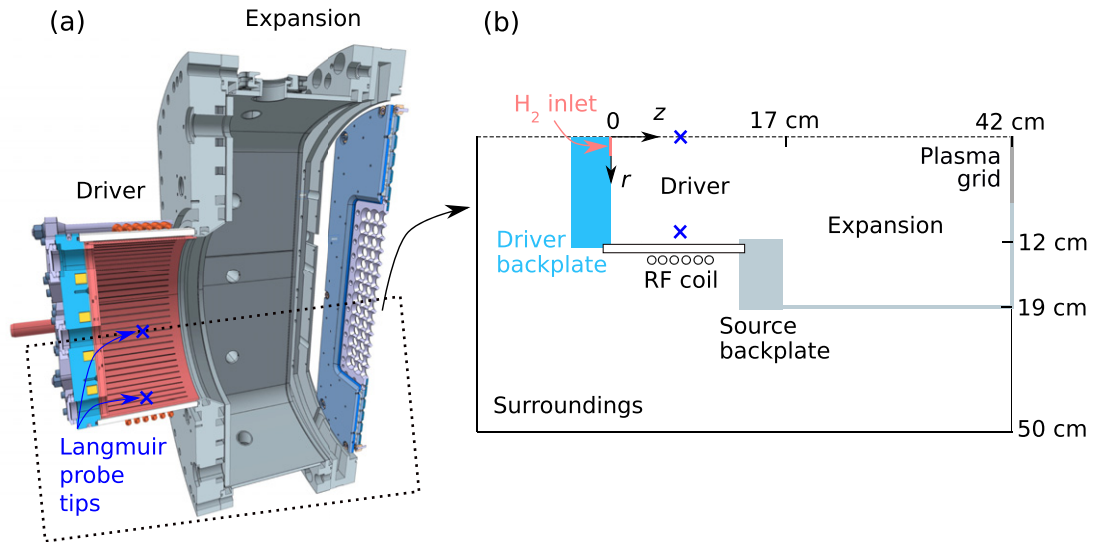
**Figure 1.** (a) CAD drawing of the ITER prototype RF ion source at the BUG test bed [1], which serves as basis for the 3D electromagnetic model simulation domain to calculate the network losses [30]. (b) 2D cylindrically symmetric simulation domain of the self-consistent RF power coupling model. Reproduced with permission from [31].

this end the ITER prototype RF ion source [1], which operates at a driving frequency of 1 MHz with RF powers of up to 100 kW and gas pressures of 0.3 Pa, is used as a representative RF ion source for setting up and validating the model. The self-consistent model is described in section 2, where subsections 2.1, 2.2 and 2.3 describe the general modeling approach, the RF power coupling and the neutrals, respectively. The main part of this work is the model validation in section 3, where subsections 3.1, 3.2 and 3.3 are devoted to show the successful validation, as well as to reveal the mechanisms of the RF power coupling and the impact of neutral depletion, respectively. Finally, a conclusion is drawn in section 4.

## 2. Model description

### 2.1. General modeling approach and simulation domain

In an inductively coupled plasma a sinusoidal current flows over an RF coil and in this way excites a time dependent electromagnetic RF field. This field develops a spatial distribution in the region occupied by plasma as well as in the immediate surroundings of the discharge. The RF field couples to the plasma electrons. In this work this coupling is described self-consistently, i.e. the electric and magnetic forces (resulting from the RF field) acting on the electrons are considered in time and space. From this follows that the spatial distribution of the macroscopic quantities (densities, fluxes and temperatures) of the charged and neutral particles species are calculated model outputs rather than inputs. Beyond the power absorbed by the plasma $P_{pl}$ (calculated from the spatially dependent macroscopic quantities) also the applied RF coil current amplitude $I_{RF}$ is an output of the calculation. Since only a negligibly small part of the total RF power provided by the RF generator $P_{RF}$ is radiated away, the active power balance reads

$$P_{RF} = P_{pl} + \frac{1}{2}R_{net}I_{RF}^2. \tag{2}$$

Herein $R_{net}$ is the network resistance, which accounts for the losses in the RF network. In equation (2) the total RF power is a known set value, whereas all terms on the right-hand side are unknown. Hence in a first step $R_{net}$ is calculated. This is done with a 3D electromagnetic model to resolve eddy currents and Joule heating in the various network components, without plasma being present. Note that this implies a neglect of the impact of possible plasma screening on $R_{net}$. However, this is consistent with the measurement procedure of the RF power transfer efficiency in the experimental setup used for the model validation [9]. The CAD drawing as shown in figure 1(a) serves as a basis for the simulation domain of the 3D electromagnetic model, where only the driver region is included. The details of this model are discussed elsewhere [30].

The self-consistent description of the power coupling between the RF fields and the plasma is realized on a 2D cylindrically symmetric simulation domain, which is shown in figure 1(b). Exploiting the cylindrical symmetry of the driver, where the RF coupling takes place, greatly enhances the model's numerical efficiency. The description of the neutrals and charged particles in the discharge is based on the fluid theory, where transport equations for the macroscopic quantities density, flux and temperature are solved. Together with the description of the RF fields via Maxwell's equations, which are solved along, useful insight about the working principle of the RF power coupling mechanism can be gained. Note that this is not possible with 0D global models, as used in [23, 24], because of the missing spatial resolution. A drawback of the fluid approach is the missing information about the velocity distribution function (a Maxwell–Boltzmann distribution is assumed as input), which is calculated in kinetic models. However, due to the large discharge volume and the high electron densities in RF ion sources, kinetic models

(e.g. particle in cell models) are numerically too expensive because of the prohibitive microscopic length- and time-scales.

The inputs needed for the fluid model are gas type, where presently only hydrogen is implemented, simulation domain, as shown in figure 1(b), set value of the $H_2$ influx at the inlet as well as transparency of the grid system at the outlet, set $P_{RF}$, driving frequency $f$ and $R_{net}$. The latter is either directly measured or obtained from the 3D electromagnetic model. Note that the model does not include any external magnetic fields such as filter and cusp fields, since these fields break the cylindrical symmetry and hence cannot be included in a 2D cylindrically symmetric simulation domain. The mathematical description of the model is based on the equations and boundary conditions given in [31, 32]. Also the relevant collisional processes including the respective cross-sections are discussed there. However there are important differences in the description of the RF power coupling as well as of the neutrals, as will be explained in subsections 2.2 and 2.3.

## 2.2. Self-consistent modeling of power coupling in RF ion sources

It typically takes up to $10^{-1}$ s for the plasma to reach a quasi-steady state at a neutral particle filling pressure $p_{fill}$ of 0.3 Pa, because of the neutrals slow temporal behavior. This is five orders of magnitude larger than the RF time scale. Hence for the simulation time not to become prohibitively long, the time harmonic approximation is used, i.e. $X(r, t) = \text{Re}\{\tilde{X}(r)e^{i\omega t}\}$ is assumed, where the complex amplitudes of the RF fields and plasma current density are denoted by $\tilde{B}$, $\tilde{E}$ and $\tilde{J}$, respectively. In this way the simulation time is of the order of hours instead of several weeks for one run, which would be necessary for a fully time resolved model. It has been verified with a simplified 1D implementation of the model including neutrals and a 2D implementation with a stationary neutrals background, that the results obtained with the time harmonic approximation are in good agreement (typical deviations less than 10%) with the ones from the fully time dependent models. Because of the assumed cylindrical symmetry (i.e. $\partial_\varphi \equiv 0$) $\tilde{B} = (\tilde{B}_r, 0, \tilde{B}_z)^\top$, $\tilde{E} = (0, \tilde{E}_\varphi, 0)^\top$ and $\tilde{J} = (0, \tilde{J}_\varphi, 0)^\top$. Maxwell's equations in quasi-magnetostatic approximation are solved for $\tilde{B}$ and $\tilde{E}$ in the surroundings (where vacuum is assumed) as well as in the discharge region.

$$\nabla \times \tilde{B} = \mu_0 \tilde{J}, \quad (3)$$

$$\nabla \times \tilde{E} = -i\omega \tilde{B}. \quad (4)$$

Herein $\mu_0$ and $\omega = 2\pi f$ denote the vacuum permeability and the angular driving frequency, respectively. The RF system is excited by a surface current amplitude $J_{surf,\varphi} = I_{RF}/\pi d_{coil}$ at the RF coil circumference with length $\pi d_{coil}$, where $d_{coil} = 6$ mm is the diameter of the RF coil tube. The RF current amplitude $I_{RF}$ is controlled by an integral controller, such that the power balance (2) is fulfilled at any time. At the conducting structure, such as the driver- and source backplates and the radial expansion wall, the electric RF field component tangential to the wall is set to zero.
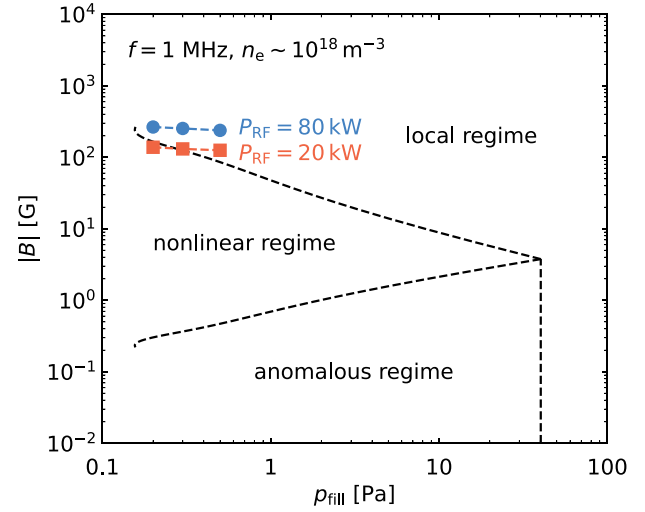


**Figure 2.** Regions of anomalous, nonlinear and local RF skin effect regime at a fixed driving frequency $f = 1$ MHz for various filling pressures $p_{fill}$ and magnetic RF field strengths $|B|$. The RF ion source operates mostly in the high magnetic RF field region of the local regime. Reproduced from [32]. © IOP Publishing Ltd. CC BY 4.0.

The power coupling to the plasma electrons is described in the electron momentum and energy transport equations. The electron momentum transport equation in convective form reads

$$m_e n_e \left( \partial_t u_e + (u_e \cdot \nabla) u_e \right) = -n_e e E + n_e F_L - m_e n_e \nu_{e,n} u_e - \nabla n_e e T_e - \nabla \cdot \underline{\underline{\pi}}_e, \quad (5)$$

where the electron mass, density and elementary charge are denoted by $m_e$, $n_e$ and $e$, respectively. The terms on the right-hand side describe the forces acting on the electrons: the electric force $-eE$, the Lorentz force $F_L = -eu_e \times B$, the friction force $-m_e\nu_{e,n}u_e$ and the gradient pressure force $-\nabla n_e e T_e$, respectively. In the friction force the elastic momentum transfer frequency for collisions between electrons and neutrals is denoted by $\nu_{e,n} = X_{e,a}n_a + X_{e,m}n_m$. Here the electron temperature dependent rate coefficients $X_{e,a}$ and $X_{e,m}$ are calculated using the elastic momentum transfer cross-sections as cited in [31, 32]. Note that since the electron density in the driver of the negative ion source is not substantially larger than $10^{18}$ m$^{-3}$, Coulomb collisions are found to be negligible. The divergence of the stress tensor is approximated as

$$\nabla \cdot \underline{\underline{\pi}}_e \approx -\mu_e \left( \nabla^2 u_e + \frac{1}{3}\nabla(\nabla \cdot u_e) \right), \quad (6)$$

where a uniform dynamic viscosity $\mu_e$ is assumed.

To decide what terms of equation (5) are important in the operation regime of an RF ion source, the three possible skin effect regimes anomalous, nonlinear and local, as classified in [19] and applied in [32] are reviewed. In which regime a specific discharge is located depends on the plasma parameters (electron density and temperature) as well as on the applied driving frequency $f$, filling pressure $p_{fill}$ and RF magnetic field strength $|B|$. For the ITER RF prototype ion source this is illustrated at a fixed driving frequency $f = 1$ MHz in figure 2.

The regime that is described most simple (and hence used ubiquitously) is the local regime at low magnetic RF fields, i.e. the region at large $p_{\text{fill}} \gtrsim 40$ Pa and low $|B| \lesssim 3$ G. Here collisions dominate, wherefore the divergence of the stress tensor can be neglected when compared to the electron pressure gradient. At low $|\tilde{B}|$ the RF Lorentz force is small compared to the electric force, wherefore it can be neglected as well in this regime. This leads to Ohm's law, where a local RF plasma conductivity relates the RF plasma current density to the RF electric field, i.e. the cold plasma approximation of an unmagnetized plasma [20].

Gradually decreasing the filling pressure at low RF magnetic fields changes the skin effect toward the anomalous regime. There are two seemingly different possibilities to describe the RF power coupling in this regime. However, these have in essence the same effect. The first one was derived by Vahedi, where $\nu_{\text{e,n}}$ is augmented by a stochastic collision frequency to account for collisionless heating [20, 25]. Another possibility was proposed by Hagelaar [28, 29]. It leaves $\nu_{\text{e,n}}$ untouched but involves a non-local approximation for the electron viscosity $\mu_{\text{e,stoc}}$ to mimic stochastic heating. In any case, since the typical RF magnetic fields in this regime are weak, the RF Lorentz force is negligible.

However, when $|B|$ is increased at low $p_{\text{fill}}$, the discharges enter the nonlinear skin effect regime or turn back to the local regime at even larger $|B|$. This is the case for the operation points of the ITER prototype RF ion source, which are indicated in figure 2 for two different RF generator power levels. Due to the high applied RF coil current amplitudes of several 100 A, the typical RF magnetic fields are well above 100 G. In this case the Lorentz force $F_{\text{L}}$ becomes comparable to the other forces, wherefore it has to be retained in the electron momentum transport equation. Also because of the large RF magnetic field $|B|$, stochastic heating might be suppressed [33]. The straight electron trajectory approach, which is a crucial assumption in the descriptions of the anomalous regime of Vahedi [25] and Hagelaar [17, 28, 29] must consequently fail in the nonlinear regime. A more appropriate picture is that electrons, which are fully magnetized by the RF magnetic field gyrate on small orbits (typical Larmor radii smaller than 1 mm) around the RF field lines and are transported through the magnetic RF field via collisions, as described by the local skin effect regime. This justifies the use of a local collisional viscosity, as derived in [34], i.e.

$$\mu_{\text{e,coll}} = \frac{2}{3} \frac{n_{\text{e}} e T_{\text{e}}}{\nu_{\text{e,n}}}. \quad (7)$$

Also note that the validity of the fluid approach is extended to unusually low pressures of around 0.3 Pa by the strong RF magnetic field [33].

Equation (5) is decomposed in its $r$, $\varphi$ and $z$-components. Starting with the $\varphi$-component, which is solved for the complex amplitude of the electron velocity $\tilde{u}_{\text{e},\varphi}$, application of the time harmonic approximation yields

$$\text{i}\omega n_{\text{e}} m_{\text{e}} \tilde{u}_{\text{e},\varphi} = -n_{\text{e}} e \tilde{E}_\varphi + n_{\text{e}} \tilde{F}_{\text{L},\varphi} - n_{\text{e}} m_{\text{e}} \nu_{\text{e,n}} \tilde{u}_{\text{e},\varphi} - [\nabla \cdot \tilde{\underline{\underline{\pi}}}_{\text{e}}]_\varphi, \quad (8)$$

where

$$\tilde{F}_{\text{L},\varphi} = -e \left( u_{\text{e},z} \tilde{B}_r - u_{\text{e},r} \tilde{B}_z \right), \quad (9)$$

and

$$[\nabla \cdot \tilde{\underline{\underline{\pi}}}_{\text{e}}]_\varphi = -\mu_{\text{e,coll}} \left( \nabla^2 \tilde{u}_{\text{e},\varphi} - \frac{\tilde{u}_{\text{e},\varphi}}{r^2} \right). \quad (10)$$

Note that the advection term on the left-hand side of equation (8) has been dropped, since it is found to be negligibly small compared to all the other terms on the right-hand side. From $\tilde{u}_{\text{e},\varphi}$ as obtained from equation (8) follows the complex amplitude of the electron current density $\tilde{J}_\varphi = -e n_{\text{e}} \tilde{u}_{\text{e},\varphi}$.

For the $r$- and $z$-components a drift–diffusion type flux is derived from equation (5). Neglecting inertia and advection on the left-hand side, as well as the divergence of the stress tensor on the right-hand side [34] yields

$$n_{\text{e}} \boldsymbol{u}_{\text{e}} = \frac{e}{m_{\text{e}} \nu_{\text{e,n}}} n_{\text{e}} \nabla \phi - \frac{e}{m_{\text{e}} \nu_{\text{e,n}}} \nabla n_{\text{e}} T_{\text{e}} + \frac{n_{\text{e}}}{m_{\text{e}} \nu_{\text{e,n}}} \bar{\boldsymbol{F}}_{\text{L}}, \quad (11)$$

where the RF-averaged Lorentz force

$$\bar{\boldsymbol{F}}_{\text{L}} = f \int_0^{1/f} - e \boldsymbol{u}_{\text{e}} \times \boldsymbol{B} \, \text{d}t = -e \frac{1}{2} \text{Re}\{\tilde{u}_{\text{e},z} \tilde{B}_z^* \boldsymbol{e}_r - \tilde{u}_{\text{e},\varphi} \tilde{B}_r^* \boldsymbol{e}_z\}. \quad (12)$$

Herein $\text{Re}\{\cdot\}$, the asterisk, $\boldsymbol{e}_r$ and $\boldsymbol{e}_z$ denote the real part, complex conjugation and the unit vector in $r$ and $z$ direction, respectively. Note that the $\varphi$-component of $\bar{\boldsymbol{F}}_{\text{L}}$ vanishes in the process of RF averaging, wherefore $\bar{\boldsymbol{F}}_{\text{L}}$ acts such as to push the plasma electrons radially and axially away from the RF coil.

The electron energy transport equation reads

$$\partial_t \left( n_{\text{e}} \frac{3}{2} e T_{\text{e}} \right) + \nabla \cdot \boldsymbol{Q}_{\text{e}} = \mathcal{P}_{\text{ind}} - e n_{\text{e}} \boldsymbol{u}_{\text{e}} \cdot (-\nabla \phi) - \mathcal{P}_{\text{e}}, \quad (13)$$

where

$$\boldsymbol{Q}_{\text{e}} = \frac{5}{2} e T_{\text{e}} n_{\text{e}} \boldsymbol{u}_{\text{e}} - \kappa_{\text{e}} \nabla e T_{\text{e}} + \underline{\underline{\pi}}_{\text{e}} \boldsymbol{u}_{\text{e}}, \quad (14)$$

and the thermal heat conductivity coefficient

$$\kappa_{\text{e}} = \frac{5}{2} \frac{n_{\text{e}} e T_{\text{e}}}{m_{\text{e}} \nu_{\text{e,n}}}. \quad (15)$$

The inductive heating power per unit volume

$$\mathcal{P}_{\text{ind}} = \frac{1}{2} \text{Re}\{\tilde{J}_\varphi \tilde{E}_\varphi^*\}. \quad (16)$$

Consequently the total power absorbed by the plasma is

$$P_{\text{pl}} = \int_{V_{plasma}} \mathcal{P}_{\text{ind}} \, \text{d}V. \quad (17)$$

Considering equation (8) for the positive ions i $\in \{\text{H}^+, \text{H}_2^+, \text{H}_3^+\}$ leads to the conclusion that because of the comparatively large $m_{\text{i}}$ the ionic RF velocity $\tilde{u}_{\text{i},\varphi}$ and hence the contribution of the ions to the plasma current density is negligible. Consequently direct RF heating of the ions is not relevant. From equation (12) applied to the ions follows that also the RF-averaged Lorentz force acting on the ions is negligible, wherefore the ions are not magnetized by the RF magnetic field. Hence the ion momentum transport equation as given in [32] applies.

## 2.3. Modeling neutral depletion in RF ion sources

Instead of the constant neutral background, which is assumed in [32], a fluid description of the atoms and molecules is necessary to capture neutral depletion and its impact on the RF power coupling. Hence for the hydrogen atoms and molecules $n \in \{a, m\}$ the Navier–Stokes equations are solved [17]. The particle transport equation

$$\partial_t n_n + \nabla \cdot (n_n \boldsymbol{u}_n) = \mathcal{R}_n, \tag{18}$$

is solved for the particle density $n_n$. The reaction rates $\mathcal{R}_n$ are obtained using the processes as specified in [32]. To obtain the fluid velocity $\boldsymbol{u}_n$, the momentum transport equation

$$m_n n_n \left( \partial_t \boldsymbol{u}_n + (\boldsymbol{u}_n \cdot \nabla) \boldsymbol{u}_n \right) = -\nabla n_n k_B T_n - \nabla \cdot \underline{\underline{\pi_n}}$$
$$- \sum_{j \neq n} \frac{m_n m_j}{m_n + m_j} n_n \nu_{n,j}$$
$$\times (\boldsymbol{u}_n - \boldsymbol{u}_j). \tag{19}$$

The last term on the right-hand side accounts for elastic collisions between the neutrals and other species, denoted by the index j. The divergence of the stress tensor

$$\nabla \cdot \underline{\underline{\pi_n}} \approx -\mu_{n,coll} \left( \nabla^2 \boldsymbol{u}_n + \frac{1}{3} \nabla (\nabla \cdot \boldsymbol{u}_n) \right). \tag{20}$$

Here again the stress tensor has been simplified by assuming a uniform dynamic viscosity

$$\mu_{n,coll} = \frac{2}{3} \frac{m_n n_n k_B T_n}{\sum_j \frac{m_n m_j}{m_n + m_j} \nu_{n,j}}, \tag{21}$$

as derived in [17]. The energy transport equation is solved for the neutral temperatures $T_n$ and reads

$$\partial_t \left( n_n \frac{3 + \zeta_{n,int}}{2} k_B T_n \right) + \nabla \cdot \boldsymbol{Q}_n = \mathcal{P}_n. \tag{22}$$

Here the internal degrees of freedom $\zeta_{a,int} = 0$ and $\zeta_{m,int} = 3$ because in hydrogen atoms there are no internal degrees of freedom, whereas in hydrogen molecules there are two rotational and one vibrational modes available for energy storage. The neutral volume power losses due to elastic collisions and directed energy transfer [35] as well as due to inelastic collisions (as given in [32]) are denoted by $\mathcal{P}_n$. The neutral energy flux is

$$\boldsymbol{Q}_n = \frac{5 + \zeta_{n,int}}{2} k_B T_n n_n \boldsymbol{u}_n - \kappa_n \nabla k_B T_n, \tag{23}$$

where the thermal conductivity coefficient

$$\kappa_n = \frac{\frac{5 + \zeta_{n,int}}{2} n_n k_B T_n}{\sum_j \frac{m_n m_j}{m_n + m_j} \nu_{n,j}}. \tag{24}$$

Boundary conditions for the neutrals particle and energy fluxes are derived from kinetic considerations, following the approach in [17]. The particle flux perpendicular to the discharge walls is

$$n_n \boldsymbol{u}_n \cdot \hat{n} = n_n u_{n,eff} - (1 - t_{grid}) \Gamma_{n,back} - \Gamma_{n,inj}. \tag{25}$$

Here the effective forward flux

$$n_n u_{n,eff} = \frac{n_n}{2\pi^{1/2}} \left( \pi^{1/2} u_{n,\perp} \left( 1 + \mathrm{erf} \left( \frac{u_{n,\perp}}{v_{n,p}} \right) \right) \right.$$
$$\left. + v_{n,p} \exp \left( \frac{-u_{n,\perp}^2}{v_{n,p}^2} \right) \right), \tag{26}$$

where $v_{n,p} = \sqrt{2k_B T_n/m_n}$. The effective forward flux is reduced by a backflux

$$\Gamma_{n,back} = \sum_j \frac{A_j}{A_n} p_{j,n} n_j u_{j,eff}, \tag{27}$$

which is caused by particles of species j with mass numbers $A_j$ impinging onto the discharge walls and having a wall recombination probability $p_{j,n}$, as specified in [31]. The molecular flux injected at the inlet $\Gamma_{n,inj}$ and the transparency of the grid system $t_{grid}$ are deduced from experimental measurements [31]. The energy flux perpendicular to the discharge walls is calculated in a similar manner than the particle flux, i.e.

$$\boldsymbol{Q}_n \cdot \hat{n} = n_n u_{n,eff} U_n - (1 - t_{grid}) \Theta_{n,back} - \Theta_{n,inj}, \tag{28}$$

where

$$n_n u_{n,eff} U_n = \frac{n_n m_n}{8\pi^{1/2}} (\pi^{1/2} u_{n,\perp} (3v_{n,p}^2 + 2u_{n,\perp}^2)$$
$$\times \left( 1 + \mathrm{erf} \left( \frac{u_{n,\perp}}{v_{n,p}} \right) \right)$$
$$+ \frac{n_n m_n}{8\pi^{1/2}} \left( 2v_{n,p} (v_{n,p}^2 + u_{n,\perp}^2) \right.$$
$$\times \left. \exp \left( \frac{-u_{n,\perp}^2}{v_{n,p}^2} \right) \right)$$
$$+ n_n u_{n,eff} \left( 1 + \frac{\zeta_{n,int}}{2} \right) k_B T_n, \tag{29}$$

and

$$\Theta_{n,back} = \sum_j \frac{A_j}{A_n} p_{j,n} n_j u_{j,eff} \left( (1 - \alpha_{j,n}) U_j + \alpha_{j,n} \right.$$
$$\times \left. \left( 2 + \frac{\zeta_{n,int}}{2} \right) k_B T_{wall} \right). \tag{30}$$

The energy flux at the inlet is

$$\Theta_{m,inj} = \Gamma_{m,inj} \left( 2 + \frac{\zeta_{m,int}}{2} \right) k_B T_{m,inj}. \tag{31}$$

Note that the expressions (26) and (29) are more general than the ones given in [17, 21], where $u_{n,\perp} \ll v_{n,p}$ is assumed.

## 3. Model validation

The model validation is done with the ITER RF prototype ion source [1]. To diagnose its driver plasma, two Langmuir probes are used: one in the driver center and the other in the RF heating
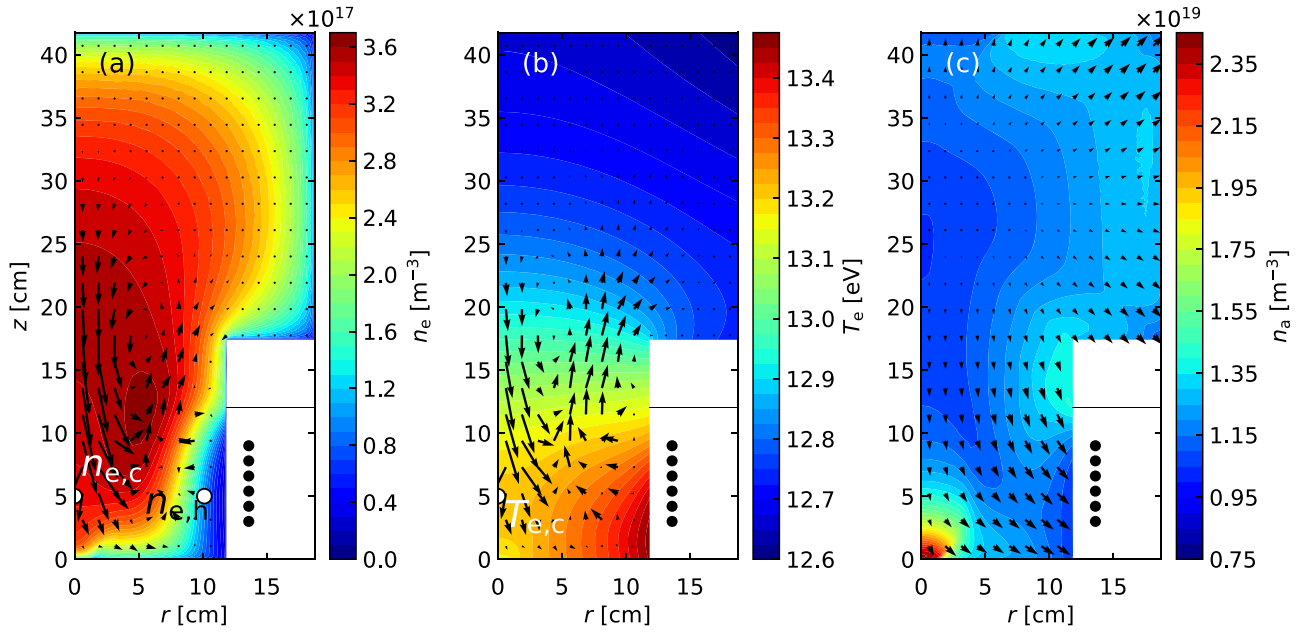
**Figure 3.** Spatial profiles of the modeled electron density (a), electron temperature (b) and atomic density (c), obtained at a filling pressure of 0.3 Pa and RF generator power of 60 kW. The direction and magnitudes of the electron flux $n_e\boldsymbol{u}_e$, electron energy flux $\boldsymbol{Q}_e$ and atomic flux $n_a\boldsymbol{u}_a$ are indicated by arrows.
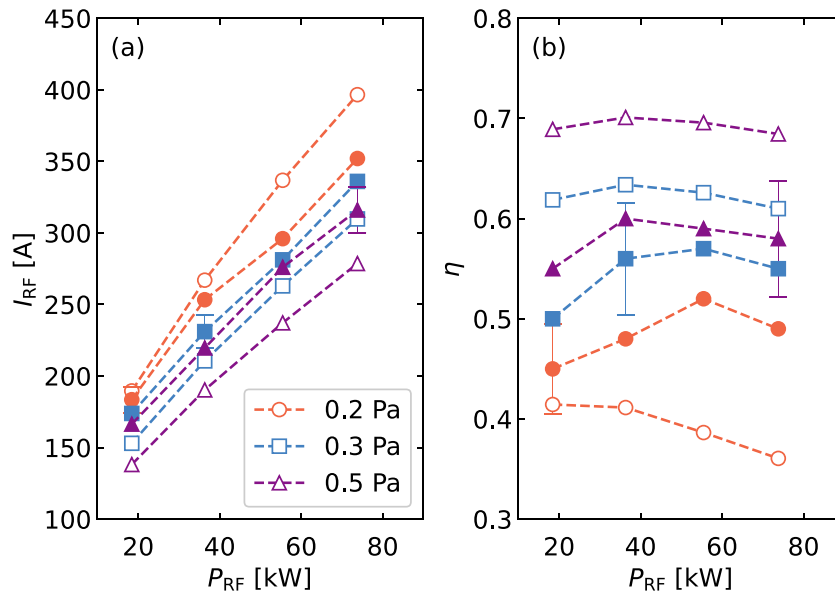


**Figure 4.** (a) RF coil current amplitude $I_{RF}$ and (b) RF power transfer efficiency $\eta$ as a function of the generator power $P_{RF}$ for three different filling pressures. Full symbols are experimentally obtained values, whereas open symbols are values calculated by the model.

zone, as marked in figure 1. From the Langmuir probe diagnostic the plasma density in the center of the driver $n_{e,c}$ and the one in the RF heating zone $n_{e,h}$ as well as the electron temperature in the driver center $T_{e,c}$ are inferred (see also marked positions in figure 3). The RF coil current amplitude $I_{RF}$ is obtained from a current transformer installed at the RF coil feedline. Details about the experimental setup and the used diagnostics for model validation are described elsewhere [9]. Note that for the validation the experimentally determined network resistance $R_{net}$ is used, since the geometry of the experimental setup does not change during the validation studies. For a detailed

discussion on the modeling of the network losses in the ITER RF prototype ion source, see [30].

Figure 3 shows results obtained from the model at a filling pressure of 0.3 Pa and an RF generator power of 60 kW. Shown in plot (a) is the electron density, which has its radially slightly off-central maximum value of around $3.6 \times 10^{19}$ m$^{-3}$ in the transition zone between driver and expansion region. The electron particle flux, indicated by the arrows forms a vortex type structure, as already seen in the discharges investigated in [32]. The electron density in the part of the driver close to the RF coil is considerably decreased by the RF Lorentz
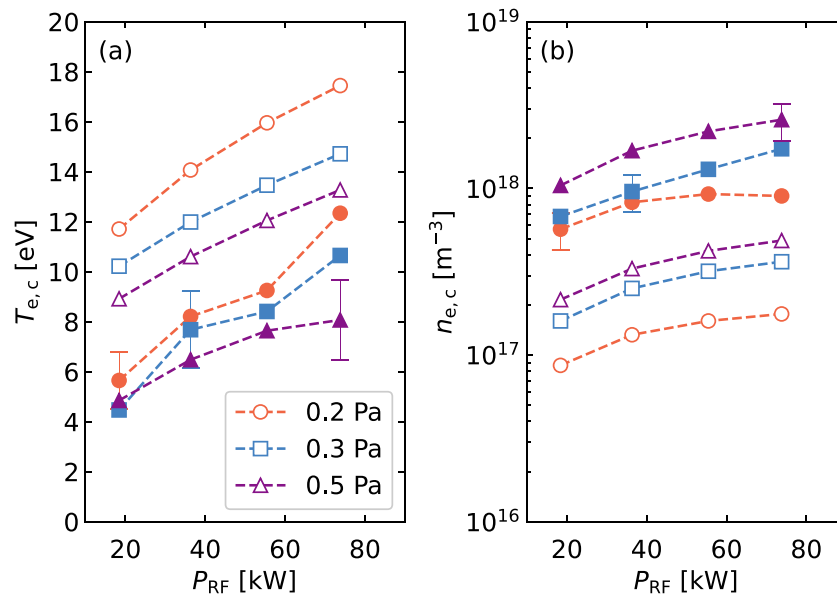
**Figure 5.** (a) Central electron temperature $T_{e,c}$ and (b) density $n_{e,c}$ as a function of the generator power $P_{RF}$ for three different filling pressures. Full symbols are experimentally obtained values, whereas open symbols are values calculated by the model.

force. The electron temperature, as shown in (b), has a maximum of around 13.4 eV close to the RF coil and decreases only slightly toward the expansion region due to the large electron energy flux, which also forms a vortex. The atomic density shows a maximum close to the inlet, where injection of hydrogen molecules takes place. The atoms are pushed to the walls by the ions, wherefore their density increases toward the walls.

### 3.1. Power and pressure variations

Figures 4(a) and (b) show the RF coil current amplitude $I_{RF}$ and the RF power transfer efficiency $\eta$, respectively, for a variation of the total delivered power by the RF generator from $P_{RF} = 20$–$80$ kW at three different filling pressures $p_{fill} = 0.2, 0.3$ and $0.5$ Pa. Focusing first on the most typical operation point of 0.3 Pa and 60 kW, it can be seen that both modeled electrical parameters $I_{RF}$ and $\eta$ are within the error bars of their experimentally obtained counterparts. Here the typical $I_{RF} \approx 250$ A and $\eta \approx 60\%$. With increasing RF power $I_{RF}$ increases approximately linearly, whereas $\eta$ is hardly affected.

Figure 5 shows how the electron temperature and density in the driver center are affected by the RF power and pressure. As is shown in figure 5(a), the electron temperature is larger at higher RF powers. This is because of stronger depletion of the neutrals via ionization, leading to a lower neutral density and consequently to a larger $T_e$ [22]. Figure 5(b) shows the increasing electron density with RF power. This dependency can only be understood when the interplay between the neutrals and the plasma including the RF coupling mechanism is considered, as will be shown in subsection 3.3. Due to the larger plasma losses at lower pressures the plasma parameters $T_{e,c}$ and $n_{e,c}$ systematically increase and decrease, respectively. At the lower electron density a larger RF current is needed and consequently $\eta$ is decreased (cf figure 4).

There are three reasons that likely explain the apparent quantitative deviations between the calculated absolute values of the plasma parameters and the experimentally obtained ones, where the modeled $T_{e,c}$ ($n_{e,c}$) is systematically too high (low), as shown in figure 5. First, in the experiment there is a cusp field in the direct vicinity of the driver back plate, which is intended to improve the axial plasma confinement on one side. Due to the nature of this field being intrinsically 3D and highly non-uniform [31], it cannot be implemented in the current 2D cylindrically symmetric simulation domain. Hence the expected plasma density increase (and $T_e$ decrease for the same absorbed power) is not included in the present model. Second, describing the neutral atoms and molecules quantitatively correct at the low pressure regime of the RF negative ion source, where typical Knudsen numbers for the neutrals are around 0.1, is only possible using kinetic methods, such as e.g. a direct simulation Monte Carlo method, as applied in [21]. There it is shown that the highly non-Maxwellian boundary fluxes of the neutrals (mainly the atomic one) leads to less neutral depletion (i.e. larger neutral densities) as well as lower atomic temperatures. Hence this should also decrease $T_e$ and consequently increase $n_e$ at the same absorbed power. As can be seen in figures 4 and 5, the deviations between the model (where a Maxwellian distribution function is used throughout) and the experimental values are most striking at the lowest pressure of 0.2 Pa and especially at high powers, where the effect of a non-Maxwellian distribution function should be most pronounced [21]. Third, the electron energy distribution function in the model is assumed to be Maxwellian. This leads to lower rate coefficients e.g. for the electron impact ionization processes, when compared to an electron energy distribution function with a bi-Maxwellian shape, as determined by [36] at $p_{fill} = 0.3$ Pa and $P_{RF} \approx 80$ kW. Consequently, the resulting modeled electron density is too low and the temperature too high.
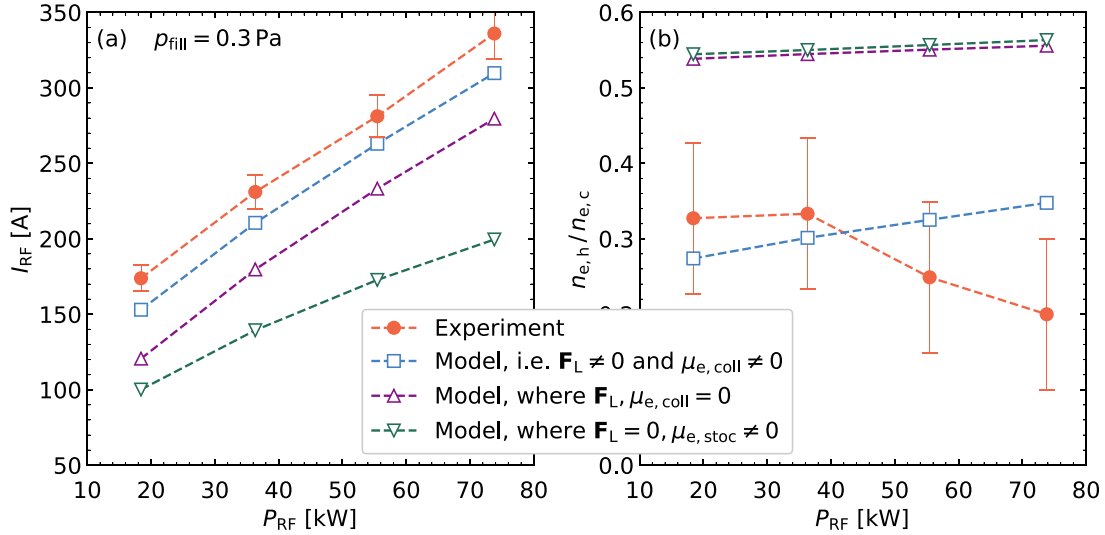
**Figure 6.** Validation of the RF power coupling mechanism by comparing different model approximations with the experimentally obtained values. (a) RF coil current amplitude $I_{RF}$ as function of the generator output power $P_{RF}$. (b) Ratio of the electron density in the RF heating zone $n_{e,h}$ to the one in the driver center $n_{e,c}$. Reproduced with permission from [31].
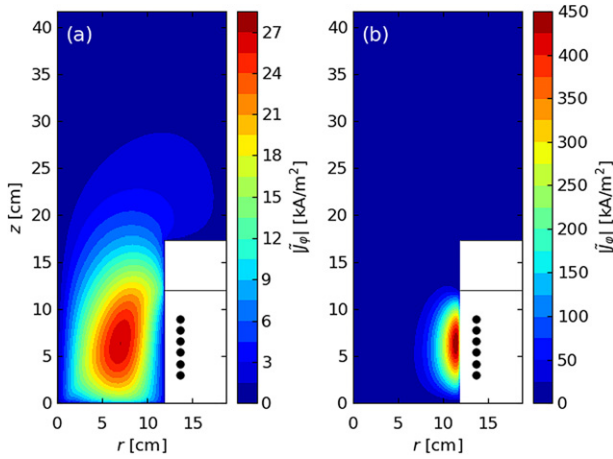


**Figure 7.** Calculated absolute value of the RF current density $|\tilde{J}_\varphi|$ at $P_{RF} = 60$ kW and $p_{fill} = 0.3$ Pa. Values in plot (a) are obtained retaining the RF Lorentz force as well as the collisional viscosity $\mu_{e,coll}$, whereas values in plot (b) are obtained neglecting both terms. Reproduced with permission from [31].

### 3.2. Investigating the RF power coupling mechanism

Figure 6 shows a comparison of different model approximations with the experimentally obtained values. In figure 6(a) is shown the RF coil current amplitude $I_{RF}$ for a varying RF generator power $P_{RF}$, whereas figure 6(b) shows the corresponding ratios of the electron densities in the RF heating zone and the driver center. Results obtained from the model using a momentum transport equation that is consistent with the local skin effect regime at large magnetic fields (i.e. RF Lorentz force $F_L$ as well as the local collisional viscosity $\mu_{e,coll}$ used) fit nicely with experimentally obtained absolute values. In this case the ratio between the heating zone and central plasma density as obtained from the model are almost constant at 0.3 Pa in agreement with the experimentally

obtained ones, for almost all powers. For comparison, approximations assuming the wrong skin effect regime are considered as well. When the local regime at low RF magnetic fields is used (i.e. cold plasma approximation), the plasma compression is missing, as evident from the large $n_e$-ratios in figure 6(b), since the RF Lorentz force is not accounted for. Consequently the RF coil current is lower ($\eta$ is higher) since more electrons are heated. Assuming the anomalous regime in the model, i.e. neglecting the RF Lorentz force and using the non-local approximation $\mu_{e,stoc}$ to mimic stochastic heating, shifts the model results even further away from the experimentally obtained values. This is because the introduced diffusion of the RF current density increases the RF heating zone beyond the classical local RF skin depth.

It was found numerically that when solely the RF Lorentz force is accounted for (also combined with $\mu_{e,stoc}$), no stationary solution is obtained, since the RF-averaged Lorentz force from equation (12) is strongly compressing the plasma radially inwards and pushing it out of the driver [17]. However, it is found in this work that the local collisional expression for the viscosity $\mu_{e,coll}$, as given by equation (7), mitigates the RF-averaged Lorentz force. This becomes evident from figure 7, where the RF current density is shown. Figure 7(a) shows the calculated result, when the RF Lorentz force and the collisional viscosity $\mu_{e,coll}$ are retained. The mechanism produces steady-state numerical results, because the viscosity leads to an RF current density which diffuses radially inwards. This in turn decreases the absolute value of the RF current density, which weakens the compression by the RF-averaged Lorentz force, as is evident from equation (12). Figure 7(b) shows the RF current density for the local collisional case without accounting for the RF Lorentz force and viscosity (cold plasma approximation). Here the RF current density shows the classical local RF skin effect without diffusion of the RF current density. Consequently, its maximum value is by more than one order of magnitude larger than in the case shown in figure 7(a).
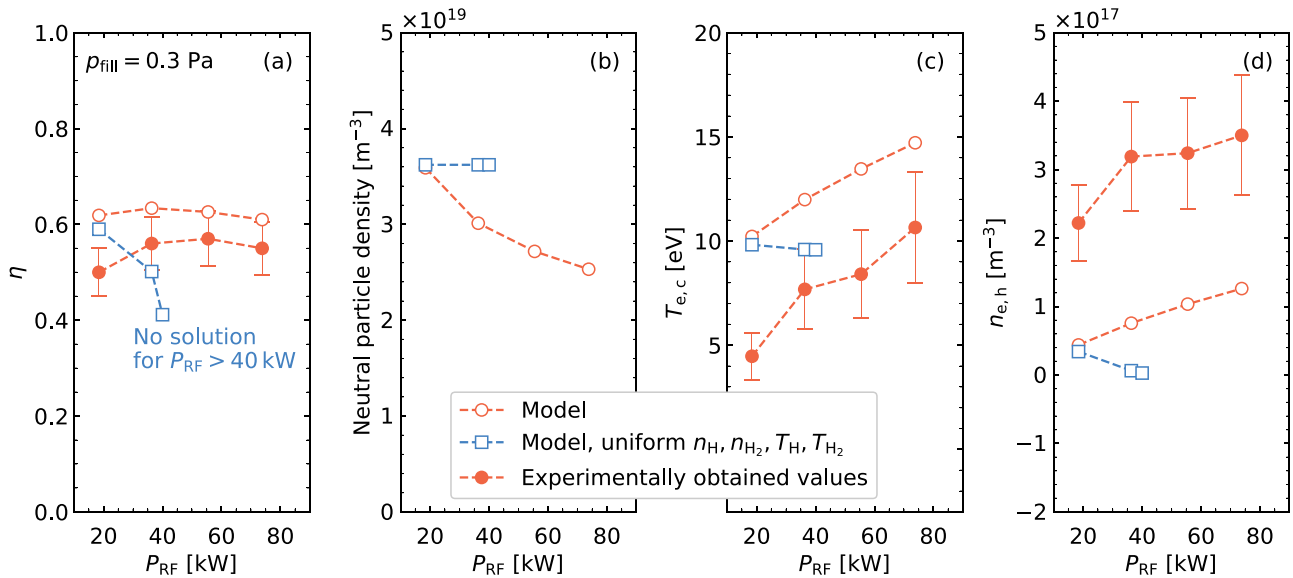
**Figure 8.** Comparison of (a) the RF power coupling efficiency $\eta$, (b) neutral particle density $n_H + n_{H_2}$, (c) electron temperature in the driver center and (d) electron density in the RF heating zone for a uniform neutral background versus a description of the neutral particle fluids via particle-, momentum- and energy transport equations (simply labeled as 'model').

### 3.3. Impact of neutral depletion on the RF power coupling mechanism

To study the impact of neutral depletion on the RF power coupling, a comparison with and without describing the neutral atoms and molecules as fluids (i.e. solving the respective particle-, momentum- and energy transport equations) is performed. The results of this comparison are shown in figure 8.

In the case of uniform atomic and molecular densities and temperatures the RF power transfer efficiency $\eta$ decreases with increasing power leading to no numerical solution for $P_{RF} > 40$ kW, as shown in figure 8(a). In contrast to that the obtained numerical solution is in good agreement with the experimentally obtained values of $\eta$ when the neutrals are described by the Navier–Stokes equations, as outlined in subsection 2.3.

The behavior of the neutrals is shown in figure 8(b). At an RF power of 20 kW both models show the same neutral particle density $n_n \approx 3.6 \times 10^{19}$ m$^{-3}$, which is corresponding to a pressure of 0.3 Pa in plasma at a temperature of $T_{H_2} \approx 600$ K. When $P_{RF}$ is increased, the neutral particle density decreases because of increasing ionization, i.e. neutral depletion sets in, leading to an increased electron temperature $T_{e,c}$, as shown in figure 8(c). Note that $T_{e,c}$ does almost not scale with power, when the neutrals are assumed as a stationary background. This is expected textbook behavior for a stationary neutrals background, where the global model plasma particle and energy balance are decoupled [37]. The decreasing neutral particle density and increasing $T_e$ yield that $\mu_{e,coll}$, as given by equation (7), increases. Hence the diffusion of the RF current density increases as well. This in turn leads to a lower absolute value of the RF current density, wherefore the compression via the RF-averaged component of the RF Lorentz force, as described by equation (12), is mitigated. From this

follows an increasing electron density in the RF heating zone with power, as shown in figure 8(d).

Because of neutral depletion, the neutral particle density during plasma operation is considerably decreased compared to the one corresponding to the filling pressure, i.e. without plasma present. Note also that at 0.3 Pa the electron pressure is comparable to the filling pressure. The calculated atomic to molecular ratio (not shown in figure 8) is around 0.5, which is in reasonable agreement with values obtained from optical emission spectroscopy and collisional radiative modeling [38].

## 4. Conclusion

In this work a self-consistent description of the RF power coupling in the regime where negative hydrogen RF ion sources are typically operated is established for the first time. By comparison to experimentally obtained electrical and plasma parameters at the ITER RF prototype ion source, it is shown that all experimentally obtained quantities scale as the numerically calculated ones.

The two main physics effects fundamental for the power coupling in RF ion sources are revealed: first, a highly nonlinear interplay between the RF Lorentz force, which tends to compress the plasma and the viscosity, which leads to diffusion of the RF current density. In this way the compression is mitigated resulting in steady state numerical solutions for the first time. Second, neutral depletion affects not only the discharge structure, but also has a profound impact on the RF power coupling due to the coupling of plasma and neutrals, which manifests in the electron viscosity. Only by accounting for this effect, steady state solutions at high power levels up to 100 kW become possible.

The remaining quantitative differences between the numerically obtained values and the ones from the experimental

setup could be attributed to 3D effects (caused by a non-uniform magnetic cusp field) that are currently not accounted for in the 2D cylindrically symmetric model. Furthermore, the Navier–Stokes fluid description of the neutrals does not account for the highly non-Maxwellian nature of the neutral particle distribution functions, resulting in deviations of the absolute values. Finally, the assumption of the Maxwellian electron energy distribution function in the model could also lead to the too low densities and too high temperatures of the electrons.

Nevertheless, because of the correct scaling of all parameters calculated by the model, it can be applied for optimizing power coupling in RF ion sources. This will exemplarily be shown in a forthcoming paper, where the model is used to find the external parameters which have the largest positive impact on the RF coupling in the ITER prototype RF ion source.

## Acknowledgments

## Data availability statement

The data that support the findings of this study are available upon reasonable request from the authors.

## ORCID iDs

D Zielke ⬤ https://orcid.org/0000-0003-4231-4350
S Briefi ⬤ https://orcid.org/0000-0003-2997-3503
S Lishev ⬤ https://orcid.org/0000-0001-5117-1561
U Fantz ⬤ https://orcid.org/0000-0003-2239-3477

## References

[1] Heinemann B *et al* 2017 *New J. Phys.* **19** 015001
[2] Toigo V *et al* 2021 *Fusion Eng. Des.* **168** 112622
[3] Zuo C, Dong L, Chen D and Chen P 2018 *AIP Conf. Proc.* **2052** 040017
[4] Lettry J *et al* 2016 *Rev. Sci. Instrum.* **87** 02B139
[5] Welton R F *et al* 2021 *AIP Conf. Proc.* **2373** 070004
[6] Ueno A, Ohkoshi K, Ikegami K, Takagi A, Shinto K and Oguri H 2021 *AIP Conf. Proc.* **2373** 040002
[7] Bacal M, Sasao M and Wada M 2021 *J. Appl. Phys.* **129** 221101
[8] Franzen P, Schiesko L, Fröschle M, Wünderlich D and Fantz U 2011 *Plasma Phys. Control. Fusion* **53** 115006
[9] Zielke D, Briefi S and Fantz U 2021 *J. Phys. D: Appl. Phys.* **54** 155202
[10] Jain P, Recchia M, Maistrello A and Gaio E 2021 Experimental investigation of RF driver equivalent impedance in the inductively coupled SPIDER ion source *Int. Conf. Ion Sources (ICIS2021)* (Vancouver, Canada)
[11] Smolyakov A I, Godyak V and Tyshetskiy Y 2001 *Phys. Plasmas* **8** 3857–60
[12] Smolyakov A I, Godyak V A and Tyshetskiy Y O 2003 *Phys. Plasmas* **10** 2108–16
[13] Sydorenko D Y, Smolyakov A I, Tyshetskiy Y O and Godyak V A 2005 *Phys. Plasmas* **12** 033503
[14] Si X-J, Zhao S-X, Xu X, Bogaerts A and Wang Y-N 2011 *Phys. Plasmas* **18** 033504
[15] Kolobov V I and Godyak V A 2017 *Plasma Sources Sci. Technol.* **26** 075013
[16] Kolobov V and Godyak V 2019 *Phys. Plasmas* **26** 060601
[17] Hagelaar G J M, Fubiani G and Boeuf J-P 2011 *Plasma Sources Sci. Technol.* **20** 015001
[18] Boeuf J P, Hagelaar G J M, Sarrailh P, Fubiani G and Kohen N 2011 *Plasma Sources Sci. Technol.* **20** 015002
[19] Froese A M, Smolyakov A I and Sydorenko D 2009 *Phys. Plasmas* **16** 080704
[20] Lieberman M A and Lichtenberg A J 2005 *Principles of Plasma Discharges and Materials Processing* 2nd edn (New York: Wiley)
[21] Kohen N 2015 Physique et modélisation d'une source d'ions négatifs pour l'injection du faisceau de neutres sur ITER *PhD Thesis* Université de Toulouse
[22] Fruchtman A 2017 *J. Phys. D: Appl. Phys.* **50** 473002
[23] Jain P, Recchia M, Cavenago M, Fantz U, Gaio E, Kraus W, Maistrello A and Veltri P 2018 *Plasma Phys. Control. Fusion* **60** 045007
[24] Jain P, Recchia M, Veltri P, Cavenago M, Maistrello A and Gaio E 2018 *IEEE Access* **6** 29665–76
[25] Vahedi V, Lieberman M A, DiPeso G, Rognlien T D and Hewett D 1995 *J. Appl. Phys.* **78** 1446–58
[26] Weibel E S 1967 *Phys. Fluids* **10** 741–8
[27] Lishev S, Schiesko L, Wünderlich D, Wimmer C and Fantz U 2018 *Plasma Sources Sci. Technol.* **27** 125008
[28] Hagelaar G J M 2008 *Plasma Sources Sci. Technol.* **17** 025017
[29] Hagelaar G J M 2008 *Phys. Rev. Lett.* **100** 025001
[30] Briefi S *et al* 2022 Determining RF network losses at the H− ion source test bed BATMAN Upgrade via 3D electromagnetic modeling (in preparation)
[31] Zielke D 2021 Development of a predictive self-consistent fluid model for optimizing inductive RF coupling of powerful negative hydrogen ion sources *PhD Thesis* Augsburg University
[32] Zielke D, Rauner D, Briefi S, Lishev S and Fantz U 2021 *Plasma Sources Sci. Technol.* **30** 065011
[33] Tuszewski M 1997 *Phys. Plasmas* **4** 1922–8
[34] Chang C H and Bose D 1999 *IEEE Trans. Plasma Sci.* **27** 1310–6
[35] Golant V E *et al* 1980 *Fundamentals of Plasma Physics* (*Wiley Series in Plasma Physics*) (New York: Wiley)
[36] McNeely P, Dudin S V, Christ-Koch S and Fantz U 2008 *Plasma Sources Sci. Technol.* **18** 014011
[37] Chabert P and Braithwaite N 2011 *Physics of Radio-Frequency Plasmas* 1st edn (Cambridge: Cambridge University Press)
[38] Briefi S *et al* 2018 *AIP Conf. Proc.* **2052** 040005